Glacial CO₂ decrease and deep-water deoxygenation by iron fertilization from glaciogenic dust

Akitomo Yamamoto[1,2], Ayako Abe-Ouchi[1,2], Rumi Ohgaito[1], Akinori Ito[1], Akira Oka[2]

[1]Japan Agency for Marine-Earth Science and Technology, Yokohama, Japan
[2]Atmospheric and Ocean Research Institute, The University of Tokyo, Kashiwa, Japan

Corresponding author: A. Yamamoto (akitomo@jamstec.go.jp)

Abstract

Increased accumulation of respired carbon in the deep ocean associated with enhanced efficiency of the biological carbon pump is thought to be a key mechanism of glacial CO₂ drawdown. Despite greater oxygen solubility due to seawater cooling, recent quantitative and qualitative proxy data show glacial deep-water deoxygenation, reflecting increased respired carbon accumulation. However, the mechanisms of deep-water deoxygenation and contribution from the biological pump to glacial CO₂ drawdown have remained unclear. In this study, we report the significance of iron fertilization from glaciogenic dust in glacial CO₂ decrease and deep-water deoxygenation using our numerical simulation, which successfully reproduces the magnitude and large-scale pattern of the observed oxygen changes from the present to the Last Glacial Maximum. Sensitivity experiments show that physical changes contribute to only one-half of all glacial deep deoxygenation whereas the other one-half is driven by iron fertilization and an increase in the whole ocean nutrient inventory. We find that iron input from glaciogenic dust with higher iron solubility is the most significant factor in enhancing the biological pump and deep-water deoxygenation. Glacial deep-water deoxygenation expands the hypoxic waters in the deep Pacific and Indian oceans. The simulated global volume of hypoxic waters is nearly double the present value, suggesting that glacial deep-water was a more severe environment for benthic animals than that of the modern oceans. Our model underestimates the deoxygenation in the deep Southern Ocean because of enhanced ventilation. The model-proxy comparison of oxygen change suggests that a stratified Southern Ocean is required for reproducing the oxygen decrease in the deep Southern Ocean. Iron fertilization and a global nutrient increase contribute to a decrease in glacial CO₂ of more than 30 ppm, which is supported by the model-proxy agreement

26 **of oxygen change. Our findings confirm the significance of the biological pump in glacial CO_2 drawdown and**

27 **deoxygenation.**

28

1 Introduction

30 The oceanic carbon cycle has been proposed as a driver of glacial–interglacial CO_2 change; however, the magnitude of glacial

31 CO_2 reduction of 80-100 ppm has yet to be fully reproduced by numerical model simulations using both an ocean general

32 circulation model (OGCM) and a biogeochemical model (Ciais et al., 2013). The oceanic soft-tissue biological pump, by which

33 the photosynthetic production, sinking, and remineralization of organic matter store dissolved inorganic carbon in the deep

34 ocean, is among the mechanisms controlling glacial-interglacial as well as future atmospheric CO_2 change (Sarmiento and

35 Gruber 2006; Sigman et al., 2010; Yamamoto et al., 2018). During glacial periods, the efficiency of the biological pump would

36 have been enhanced by biogeochemical processes (e.g. dust-borne iron fertilization (Martin, 1990) and an increase in nutrient

37 inventory associated with a sea-level drop (Broecker, 1982; Wallmann et al., 2016)), leading to the transfer of carbon from the

38 atmosphere to the deep ocean. Although changes in marine productivity during glacial periods and its relationship to the dust

39 deposition flux have been widely supported by proxy records (Kohfeld et al., 2005; Jaccard et al., 2013), there are no direct

40 proxy records of the greater accumulation of respired organic carbon. Thus, the contribution of the biological pump to glacial

41 CO_2 reduction is poorly understood.

42

43 Because the dissolved oxygen cycle is the mirror image of the biological carbon cycle (oxygen is produced by photosynthesis

44 and is utilized with consistent stoichiometry through the remineralization of sinking organic matter in the ocean interior),

45 oxygen is consumed in the ocean interior when respired organic carbon accumulates in seawater. Thus, reconstructed oxygen

46 change is useful to constrain the biological pump magnitude and respired carbon accumulation. Proxy data show that, despite

47 greater oxygen solubility due to lower sea surface temperatures (SSTs), oxygen concentrations decreased throughout the deep

48 ocean during the Last Glacial Maximum (LGM) (Jaccard and Galbraith, 2012). This indicates greater oxygen consumption

49 and respired carbon accumulation, which could have been caused by several processes including greater organic matter

50 transport into the deep ocean, increasingly restricted air-sea exchange due to sea-ice expansion, and/or more sluggish ocean

51 circulation. However, previous modeling studies have shown conflicting oxygen changes in LGM simulations (Galbraith and

52 Jaccard, 2015; Schmittner and Somes, 2016; Buchanan et al., 2016; Bopp et al., 2017; Somes et al., 2017; Galbraith and de

53 Lavergne, 2018) and the causes of the oxygen decrease in the deep ocean have not yet been fully explored.

54

55 Furthermore, because most observations provide only qualitative estimates of oxygen changes, previous model-proxy

56 comparisons have only discussed the glacial oxygen trend (oxygenation in the upper ocean and deoxygenation in the deep

57 ocean). Several recent studies using $\delta^{13}C$ in benthic foraminiferal or iodine-to-calcium ratios in planktonic foraminifera were

58 able to quantify oxygen concentration changes (Schmiedl and Mackensen, 2006; Hoogakker et al., 2015, 2018; Gottschalk et

59 al., 2016; Lu et al., 2016; Bunzel et al., 2017; Umling and Thunell, 2018). These quantitative proxy data provide firmer

60 constraints on respired carbon accumulation, such that a quantitative model-proxy comparison of oxygen change is very useful

61 for quantifying the contribution of the biological pump to glacial CO_2 drawdown.

62

63 In this study, to quantify the impact of changes in the biological pump on glacial carbon and oxygen cycles, we conducted pre-

64 industrial (PI) and LGM simulations using the coupled atmosphere–ocean general circulation model (Oka et al., 2011), aerosol

65 model (Ohgaito et al., 2018), and ocean biogeochemical model (Yamamoto et al., 2015). We focused here on the iron

66 fertilization process in enhancing the biological pump. We attempted to separately quantify iron fertilization effects from desert

67 dust and glaciogenic dust (derived from glacier erosion). Previous studies using mineral aerosol models suggest that

68 glaciogenic dust significantly contributed to an increase in the dust deposition flux at high latitudes during the LGM (e.g. the

69 glaciogenic dust derived from Patagonian glaciers increased dust deposition in the Southern Ocean (SO)) and provided a LGM

70 dust deposition flux distribution more consistent with the reported measurements (Mahowald et al., 2006; Ohgaito et al., 2018).

71 Moreover, the iron solubility in glaciogenic dust (~3%) is much higher than that in desert dust (~1%) (Schroth et al., 2009);

72 however, the higher solubility effect of glaciogenic dust on iron fertilization was not considered in previous modeling studies.

73 Glaciogenic dust is a significant source of bioavailable iron (Shoenfelt et al., 2018) and would therefore have a major impact

74 on biological productivity in high nutrient and low chlorophyll (HNLC) regions where biological productivity is limited by

75 the lack of iron. We also considered the effect of an increase in macronutrients inventory associated with a glacial sea level

76 drop of ~120 m (Broecker, 1982; Wallmann et al., 2016). A decrease in the area of continental margins reduced the burial of

77 organic matter in margin sediments, leading to increases in the global inventory of phosphate (PO_4) and nitrate (NO_3). Based

78 on a recent simulation, increases in NO_3 and PO_4 inventories by 15% can be assumed (Wallmann et al., 2016).

4

79

80   We performed several sensitivity experiments as listed in Table 1 to explore the contribution of changes in atmospheric dust

81   and nutrient inventory on glacial carbon and oxygen cycles. Moreover, our modeled oxygen changes were compared to recently

82   reported qualitative (Jaccard and Galbraith, 2012) and quantitative reconstructions (Schmiedl and Mackensen, 2006;

83   Hoogakker et al., 2015, 2018; Gottschalk et al., 2016; Lu et al., 2016; Bunzel et al., 2017; Umling and Thunell, 2018) to

84   evaluate the simulated accumulation of respired carbon. Our simulation shows that glaciogenic dust and increased nutrient

85   inventory play a crucial role in glacial CO_2 decrease and deep-water deoxygenation.

86

87   **2 Model and experiments**

88   The ocean biogeochemical cycle was calculated using the Model for Interdisciplinary Research on Climate (MIROC)-based

89   offline biogeochemical model, based on Yamamoto et al. (2015), with the implementation of an iron cycle. A one box

90   atmosphere is coupled to an offline biogeochemical model to predict atmospheric CO_2 concentration through gas exchange

91   between the atmosphere and ocean surface. For the tracer calculation, the model uses prescribed monthly output data of

92   horizontal ocean velocities, vertical diffusivity, temperature, salinity, sea surface height, sea surface wind speed, sea-ice

93   fraction, and sea surface solar radiation derived from PI and LGM simulations conducted by Oka et al. (2011) using the MIROC

94   4m AOGCM. Both PI and LGM simulations follow the PMIP2 protocol (Braconnot et al., 2007). MIROC 4m simulates the

95   weaker and shallower Atlantic Meridional Overturning Circulation (AMOC) during the LGM (see Fig. 1 in Oka et al. (2011)),

96   which is consistent with $\delta^{13}C$ distributions reported from proxy data (Curry and Oppo, 2005). The horizontal and vertical

97   resolutions of the offline biogeochemical model are the same as those in MIROC 4m.

98

99   This biogeochemical model includes two phytoplankton classes (nitrogen fixers and other phytoplankton), zooplankton,

100   particulate detritus, nitrate (NO_3), phosphate (PO_4), dissolved iron (DFe), dissolved oxygen (O_2), dissolved inorganic carbon

101   (DIC), alkalinity (ALK), two carbon isotopes (^{13}C and ^{14}C), and an ideal age tracer. The ideal age is set to zero at the surface

102   and ages at a rate of 1 yr yr^{-1} in the ocean interior. Constant stoichiometry relates the C, N, P, and DFe content of the biological

103   variables and their exchanges to inorganic variables (NO_3, PO_4, DFe, O_2, ALK, and DIC). The maximum phytoplankton growth

104 and microbial remineralization rates are assumed to increase with seawater temperature (Eppley, 1972). The iron cycle that is

105 incorporated in the biogeochemical model mainly follows Parekh et al. (2005). In addition to dust deposition, which is assumed

106 as the only DFe source in Parekh et al. (2005), sedimentary and hydrothermal DFe inputs are considered. When the DFe

107 concentration exceeds the total ligand concentration, a formulation for the DFe scavenging rate of Moore and Braucher (2008)

108 is applied. To obtain a realistic distribution of the iron-limited region, total ligand concentration, which controls the amount of

109 the free form of iron, is set to a global constant value of 0.6 µmol m^{-3} instead of the original value of 1 µmol m^{-3} (Fig. 1a).

110

111 Dust deposition flux is obtained from the monthly output data of MIROC-ESM in the PI and LGM simulations (Ohgaito et al.,

112 2018). Dust is assumed to contain a constant fraction of iron (3.5 wt%); 1% of the iron in desert dust is assumed to

113 instantaneously dissolve at the sea surface. The global DFe flux from dust in the PI is 2.7 Gmol yr^{-1} (Table 1). We used two

114 sets of LGM dust deposition flux labelled as LGMctl and LGMglac as calculated in a previous study (Ohgaito et al., 2018).

115 LGMctl is the standard LGM simulation, which has been submitted to Coupled Model Intercomparison Project Phase 5 /

116 Paleoclimate Modelling Intercomparison Project (CMIP5/PMIP4). LGMglac is identical to LGMctl, except that an additional

117 glaciogenic dust flux based on Mahowald et al. (2006) is included. In LGMctl, the dust deposition flux is underestimated in

118 North America, Eurasia, the South Pacific, the SO, and Antarctica compared to the proxy data of ice and sediment cores

119 (Kohfeld et al., 2013; Albani et al., 2014). Because glaciogenic dust increases dust deposition at high latitudes, the

120 underestimation is generally improved in LGMglac (see Ohgaito et al., 2018, for more details). The global DFe fluxes from

121 dust are 8.6 Gmol yr^{-1} and 13.9 Gmol yr^{-1} for LGMctl and LGMglac, respectively.

122

123 Present observation generally shows a lower Fe solubility at a higher Fe concentration in aerosols and a higher solubility at a

124 lower concentration (Fig. S1). A wider range of aerosol Fe solubility (from 0.2% to 48%) has been derived from observations

125 over the SO, but different types of Fe-containing minerals such as pyrogenic Fe oxides can be considered to achieve high Fe

126 solubilities (Ito et al., 2019). Thus, an assumed constant iron solubility of 2% in all types of dust could lead to overestimation

127 of a total DFe flux from different types of Fe-containing aerosols during the LGM (Muglia et al., 2017). However, a much

128 higher Fe solubility (1–42% of Fe solubility) as derived from observations for the LGM aerosols in Antarctica has suggested

129 that an assumed constant iron solubility of 1–2% for all types of dust could lead to a DFe flux underestimation during the LGM

130 (Conway et al., 2015). In LGM_glac3%, an iron solubility of 3% in glaciogenic dust is assumed (Schroth et al., 2009), such

131 that the global DFe flux is 24.5 Gmol yr^{-1}. This value is approximately 10 times larger than that of the PI simulation and is

132 larger than a recent estimation, suggesting that a quadrupling of the global DFe flux is constrained by a model-proxy

133 comparison of δ^{15}N and δ^{13}C (Muglia et al., 2018). As with the present DFe input from dust, glacial DFe input has large

134 uncertainties. As an upper estimate of the DFe flux from dust, we set the iron solubility at 10% in glaciogenic dust in

135 LGM_glac10%.

136

137 The DFe input flux from the sediments is estimated based on Moore and Braucher (2008). We assumed that the sedimentary

138 DFe flux is proportional to the flux of organic carbon reaching the sea floor. To consider the realistic bathymetry of the

139 continental shelves, the iron flux is weighted by the fraction of bottom area of the ETOPOV2 data that falls within the bounds

140 of the model grid cell. The global DFe flux from the sediments in the PI is 33.1 Gmol yr^{-1}. In the LGM simulations, the DFe

141 input from sedimentary sources changes according to the flux of organic carbon reaching the sea floor. A decrease in the DFe

142 input from sedimentary sources because of a sea-level drop is not considered. Muglia et al. (2017) showed this effect causes a

143 CO_2 increase of 15 ppm. The hydrothermal DFe flux is regulated by the ridge spreading rate, as parameterized by a constant

144 DFe/Helium ratio (Tagliabue et al., 2010). The hydrothermal DFe flux in the PI is ~8.5 Gmol yr^{-1}. In the LGM simulations,

145 the DFe input from hydrothermal sources is the same as that from PI.

146

147 The biogeochemical model was initialized from annual mean climatology data based on the World Ocean Atlas 2009

148 (WOA2009: Garcia et al., 2010a and 2010b) for dissolved NO_3, PO_4, and O_2 and the Global Ocean Data Analysis Project (Key

149 et al., 2004) for DIC and ALK. The initial DFe concentration is a constant value of 0.6 nM. For the spin-up, the last 50 years

150 of data in the MIROC PI experiments were cyclically applied to the offline ocean biogeochemical model. The model was spun

151 up for more than 3000 years with a prescribed atmospheric CO_2 concentration of 285 ppm to eliminate model drift in the global

152 inventory of all tracers. Similar to Yamamoto et al. (2015), all physical and biogeochemical tracers, except salinity and

153 dissolved iron, have correlation coefficients with observational data greater than 0.85 and normalized standard deviation values

154 between 0.7 and 1.1.

155

156 LGM experiments were run for 3000 years, following 3000 years of spin-up under PI conditions. The atmospheric CO_2

157 concentration was predicted. We increased the salinity, PO_4, and NO_3 inventory by 3% to account for the reduced ocean

158 volume because of the sea level drop. All experiments are listed in Table 1. LGM_clim uses LGM boundary conditions.

159 LGM_dust is based on LGM_clim but uses the dust deposition flux of LGMctl. Similarly, LGM_glac3% and LGM_glac10%

160 use the dust deposition flux of LGMglac, but with an iron solubility of glaciogenic dust of 3% and 10%, respectively. LGM_all

161 is similar to LGM_glac3%, but the NO_3 and PO_4 inventories are increased by 15%. This assumption is based on a recent model

162 simulation that shows a ~15% increase in nutrient inventory is caused by reduced organic matter burial in shallow sediments

163 associated with a sea level drop (Wallmann et al., 2016). In our simulations, changes in benthic denitrification were not

164 considered. Somes et al. (2017) show that a decrease in benthic denitrification because of a sea level drop reduces NO_3 loss

165 and thus leads to a larger NO_3 inventory in the LGM ocean. We analyzed the results from the last 100 years of each simulation.

166

167 **3 Results and Discussion**

168 **3.1 Glacial nutrient cycles and export production**

169 In the LGM_clim, which uses LGM climate boundary conditions, the NO_3 redistribution induced by weaker and shallower

170 AMOC reduces nutrient supply from the deep ocean to the surface (Table 2 and Fig. 2). The NO_3 concentration in the euphotic

171 zone decreases by 12% and the global export production (EP) is reduced by 0.54 Pg C yr^{-1} compared to that of the PI simulation.

172 Corresponding to the surface NO_3 decrease, significant EP decreases are found in the North Atlantic and North Pacific (Fig.

173 3a and Fig. S2). However, the surface DFe concentration slightly changes. Because these changes in DFe and NO_3 decrease

174 the iron-limited areas by 27% (Fig. 1b), the simulated LGM climate tends to mitigate the impacts of iron fertilization on

175 biological productivity and the carbon cycle.

176

8

177 To evaluate the impacts of desert and glaciogenic dust on the ocean biogeochemical cycles, we conducted sensitivity studies.

178 The DFe input from desert dust with a 1% iron solubility was applied in LGM_dust, whereas glaciogenic dust with 3% or 10%

179 iron solubility was additionally applied in LGM_glac3% or LGM_glac10%, respectively. Iron fertilization from only desert

180 dust has a limited impact on the EP. Iron fertilization from both desert and glaciogenic dust increases the EP by 0.88 Pg C yr$^-$

181 ^{1} south of 45°S whereas the EP decreases by 0.86 Pg C yr^{-1} north of 45°S, where most oceans are nitrogen-limited regions

182 (LGM_glac3% – LGM_clim; Table 2). Enhanced primary production consumes the NO_3 of the euphotic zone in the SO and

183 its anomaly is transported to the Antarctic bottom water (AABW). Subsequently, the surface NO_3 reduction in the SO is also

184 transported to low-latitude regions via surface and intermediate waters (Fig. 2), thus reducing the EP in nitrogen-limited regions

185 at low latitudes. Remarkable EP reductions occur north of the iron-limited regions of the SO (Fig. 3b). Our results demonstrate

186 that enhanced biotic carbon export in the SO is partly compensated for by reduced carbon export in low-latitude regions. From

187 the comparison between the effect of desert dust (LGM_dust – LGM_clim) and that of glaciogenic dust (LGM_glac3% –

188 LGM_dust), we found that an increase in the EP due to dust-bone iron fertilization in the SO is mainly caused by glaciogenic

189 dust (Table 2).

190

191 For 15% increases in NO_3 and PO_4 inventory associated with sea level drop (LGM_all), the EP increases globally in the

192 nitrogen-limited regions, leading to a global EP increase of 0.86 Pg C yr^{-1} (LGM_all – LGM_glac3%; Table 2). Simulated EP

193 changes from the PI are in good agreement with the paleoproductivity reconstruction (Kohfeld et al., 2013) (Fig. 3c). Among

194 the common patterns is the north-south dipole pattern in the SO with an EP decrease at higher latitudes and an EP increase at

195 lower latitudes. The EP decrease at higher latitudes is attributed to sea ice expansion and the associated reduction of surface

196 shortwave radiation (Oka et al., 2011) whereas iron fertilization increases the EP at lower latitudes. In the model, the EP

197 changes also have an east-west dipole pattern; a slight EP increase is found in the South Pacific Ocean and significant EP

198 increases occur in the South Atlantic and Indian oceans. We found that this pattern is attributed to iron fertilization by

199 glaciogenic dust. Glaciogenic dust derived from Patagonian glaciers is transported to the South Atlantic and Indian oceans by

200 the southern westerly wind; however, it is unable to reach the South Pacific (Fig. S3). Proxy data show no clear east-west

201 dipole pattern, suggesting that the model underestimates iron fertilization in the Pacific sector of the Southern Ocean. However,

202 proxy data in the South Pacific remain sparse and a quantitative comparison of EP changes between the South Atlantic and

203 South Pacific is limited. Therefore, further proxy data in the South Pacific is required for a comprehensive understanding of

204 the glacial EP changes and iron fertilization.

205

3.2 CO_2 reduction and its relationship to efficiency of the biological pump and dust flux

207 Climate change reduces the atmospheric CO_2 concentration by 26.4 ppm (LGM_clim – PI, Table 2), which is similar to that

208 of previous simulations (Chikamoto et al, 2012; Menviel et al., 2012; Kobayashi et al., 2015). Circulation changes (i.e. a

209 weaker and shallower AMOC and AABW expansion) cause DIC to decrease in the upper ocean and increase below 2000 m

210 depth, such that the vertical DIC gradient between the surface and deep oceans is enhanced (Fig. 4). The efficiency of the

211 oceanic biological pump is calculated following Ito and Follows (2005). The global mean preformed PO_4 is the difference

212 between the total globally averaged PO_4 and global mean remineralized PO_4, $P_{pref} = P_{tot} - P_{remi}$. Here, P_{pref} is the preformed

213 PO_4 concentration, P_{tot} is the total PO_4 concentration, and P_{remi} is the remineralized PO_4 concentration. The remineralized PO_4

214 is given by $P_{remi}=AOU \times R_{P:O}$, where $R_{P:O}$ is a constant phosphorous to oxygen ratio, and AOU is apparent oxygen utilization.

215 A decrease in preformed PO_4 and thus an increase in remineralized PO_4 indicate an increase in the efficiency of the oceanic

216 biological pump. Although globally integrated EP decreases, circulation change and deepening of the remineralization profile

217 due to seawater cooling (Matsumoto, 2007) reduce the preformed nutrient inventory, enhancing the efficiency of the biological

218 pump (Table 2). The enhanced accumulation of respired carbon associated with the more efficient biological pump and

219 increased CO_2 solubility from the lower SST contribute to a decreased CO_2. Notably, the AOU is different from true oxygen

220 utilization due to the air-sea disequilibrium which is on the order of 20 mmol m^{-3} in deep-water formation regions (Russell and

221 Dickson, 2003; Duteil et al., 2013). Changes in surface ocean disequilibrium between the PI and LGM simulations might lead

222 to large errors in the AOU changes (Khatiwala et al., accepted).

223

224 Iron fertilization from desert and glaciogenic dust enhances the vertical DIC gradient and causes a CO_2 reduction of 1.2 ppm

225 (LGM_dust – LGM_clim) and 15.6 ppm (LGM_glac3% – LGM_dust), respectively. Our results show that the glacial CO_2

226 reduction due to dust-bone iron fertilization is mainly driven by glaciogenic dust. A simulated total CO_2 reduction of 16.8 ppm

227   induced by iron fertilization is within the range of previous studies using OGCM or Earth system Models of Intermediate

228   Complexity (EMICs) (8-25 ppm CO_2 drawdown (Bopp et al., 2003; Parekh et al., 2006; Tagliabue et al., 2009; Oka et al.,

229   2011; Menviel et al., 2012; Lambert et al., 2015; Heinze et al., 2016; Muglia et al., 2017). DFe supply from dust also contributes

230   to the glacial CO_2 reduction through enhanced efficiency of the biological pump (Table 2). The simulated atmospheric CO_2

231   concentration is proportionally reduced to the preformed PO_4 (Fig. 5a), similar to previous simulations under the present

232   climate (Ito and Follows, 2005; Marinov et al., 2008). Figure 5b shows the CO_2 change in response to the DFe input magnitude.

233   The iron fertilization efficiency to reduce CO_2 decreases with increasing DFe flux. This nonlinear response is driven by a

234   decrease in the iron-limited areas and the associated weakening of the iron fertilization effect on EP (Fig. 5c). Because the

235   iron-limited region dramatically decreases in size and the CO_2 difference between LGM_glac3% and LGM_glac10% is small,

236   the CO_2 reduction of 20 ppm in LGM_glac10% is near the upper limit (i.e. there are no iron-limited regions and thus no

237   additional CO_2 reduction).

238

239   The simulated upper limit of CO_2 reduction resulting from iron fertilization is not a robust result because present iron models

240   have large uncertainty. While Parekh et al. (2008) show an upper limit of 10 ppm, other simulations show CO_2 decrease by

241   greater than 20 ppm (Oka et al., 2011; Muglia et al., 2017). To obtain a better understanding of the impact of iron fertilization

242   on glacial CO_2 decrease, the variability of the upper limit among iron models should be investigated in a future study.

243

244   Increases in nutrient inventory from lower sea levels drive an additional CO_2 drawdown by 16 ppm (LGM_all – LGM_glac3%).

245   We found that changes in the biological pump induced by iron fertilization and an increase in nutrient inventory contribute to

246   a glacial CO_2 decrease of more than 30 ppm. The resultant total CO_2 reduction is ~60 ppm, which our model does not reproduce

247   as the full variation in the glacial-interglacial CO_2 change. Note that changes in the sedimentation process (i.e. carbonate

248   compensation and burial-nutrient feedback) are not considered in our simulation. The simulated increase in the bottom water

249   DIC (Fig. 4) would enhance calcium carbonate dissolution in the sediments and thereby increase ocean alkalinity, leading to

250   a further CO_2 decrease (Bouttes et al., 2011; Brovkin et al., 2012; Kobayashi et al., 2018). The long-term balance between the

251   burial of organic material and nutrient input through weathering is also potentially important for the atmospheric CO_2 response

252 (Roth et al., 2014; Wallmann et al., 2016). For example, Tschumi et al. (2011) show that the nutrient-burial feedback

253 significantly amplifies the effect of an increase in the PO_4 inventory on the glacial CO_2 decrease. Menviel et al. (2012)

254 quantified the implication of ocean-sediment-lithosphere coupling for factorial experiments with an altered iron fertilization

255 and altered PO_4 inventory from transient glacial-interglacial simulations. Considering that EP increases due to iron fertilization

256 and the nutrient increase are smaller in our simulations than that in previous studies (Tschumi et al., 2011; Menviel et al.,

257 2012), the effect of burial-nutrient feedback on the glacial CO_2 reduction may be smaller than previously estimated. As

258 described in the next section, to assess the simulated accumulation of respired carbon, we compared the simulated oxygen

259 changes to qualitative and quantitative proxy records.

260

261 **3.3 Model-proxy comparison of glacial oxygen changes**

262 Compared to the compilation of qualitative and quantitative proxy records of oxygen change from the Holocene to Last Glacial

263 Maximum, LGM_clim shows an increase in oxygen for the entire SO and underestimates deoxygenation in the deep Pacific

264 and Indian oceans, in contrast to the proxy records (Fig. 6a). However, LGM_all successfully reproduces large-scale spatial

265 patterns of oxygen change, including for the SO (Fig. 6b). Moreover, the simulated changes in oxygen concentration agree

266 well with quantitative reconstructions: a 45-65 mmol m^{-3} decrease in the deep North Atlantic (Hoogakker et al., 2015), an ~30-

267 80 mmol m^{-3} decrease in the eastern equatorial Pacific (Hoogakker et al., 2018; Umling and Thunell, 2018), and a >80 mmol

268 m^{-3} in the upper SO of the Pacific sector (Lu et al., 2016). Our results clearly show the importance of iron fertilization and an

269 increase in nutrient inventory in global deep deoxygenation. These model-proxy agreements of oxygen change support the

270 simulated CO_2 decrease of 30 ppm by the biological pump. However, the reconstructed O_2 decrease of ~175 mmol m^{-3} in the

271 deep SO (Gottschalk et al., 2016) is much greater than the simulated decrease of ~30 mmol m^{-3} from LGM_all; thus, the

272 respired carbon accumulation in the deep SO is underestimated in our model. This may be one of the reasons why the glacial-

273 interglacial CO_2 change of ~100 ppm cannot be reproduced in our simulations.

274

275 To clarify the mechanism of O_2 change from LGM_all − PI, we decomposed the O_2 change into changes in saturation (O_{2sat})

276 and apparent oxygen utilization (AOU), where $\Delta O_2 = \Delta O_{2sat} - \Delta AOU$. O_{2sat} is computed from simulated seawater temperature

277 and salinity and AOU by subtracting the O_2 concentration from O_{2sat}. Ocean cooling increases O_{2sat} globally, increasing the

278 global mean value by 25.5 mmol m^{-3} (Fig. 7a). As with the O_2 change, ΔAOU shows a contrast between the upper and deep

279 oceans (Fig. 7b). At a depth of 0-800 m, the AOU decreases by 5.2 mmol m^{-3} north of 45°S, which results from the decrease

280 in biological oxygen consumption associated with EP reduction and increased ventilation (Fig. 7f). Therefore, the combined

281 effects of an O_{2sat} increase and AOU decrease contribute to an overall O_2 increase in the upper ocean. In the deep ocean (>2

282 km depth), the sum of AOU increases by 72.8 mmol m^{-3} (LGM_all in Table 2), overcoming the O_{2sat} increase, resulting in

283 deep O_2 depletion. The relationship between changes in the O_2 concentration, O_{2sat}, and AOU are consistent with that of a

284 previous simulation (Bopp et al., 2017).

285

286 The ΔAOU is also decomposed into effects of climate change (LGM_clim – PI), iron fertilization (LGM_glac3% – LGM_clim)

287 and an increase in nutrient inventory (LGM_all – LGM_glac3%). The effects of climate change, circulation change, restricted

288 air-sea gas exchange from sea-ice expansion, and deepening of remineralization due to seawater cooling leads to the AOU

289 increasing by 37.3 mmol m^{-3} in the deep ocean (Table 2). In the deep North Atlantic, the simulated water mass age is older in

290 the LGM than in the PI by up to 500 years, suggesting reduced ventilation (Fig. 7f). Therefore, significant AOU increases

291 occur (Fig. 7c). Meanwhile, in the SO and deep Pacific Ocean, an increase in ventilation tends to decrease the AOU and thus

292 partly compensates for the increase in the AOU. Regarding the effects of iron fertilization and nutrient inventory, the EP

293 changes associated with iron fertilization and an increase in nutrient inventory enhance biological oxygen consumption and

294 thus increase the AOU by 21.4 and 14.1 mmol m^{-3} in the deep ocean, respectively (Table 2 and Fig. 7d, e). In particular,

295 glaciogenic dust causes an increase in the AOU of 19.8 mmol m^{-3}. Our results demonstrate that in addition to climate change,

296 enhanced biological oxygen consumption associated with iron fertilization and increased nutrient inventory are crucial drivers

297 of glacial deoxygenation in the deep ocean. While some previous modelling studies show deep ocean oxygenation during the

298 LGM (Buchanan et al., 2016; Galbraith and Lavergne, 2018), this study and others reproduce deep ocean deoxygenation

299 (Galbraith and Jaccard, 2015; Schmittner and Somes, 2016; Bopp et al., 2017; Somes et al., 2017). The conflicting oxygen

300 change between the previous simulations can be attributed to different treatments of enhanced biological oxygen consumption

13

301 because iron fertilization and increased nutrient inventory are not considered in these simulations that fail to reproduce deep

302 deoxygenation (Buchanan et al., 2016; Galbraith and Lavergne, 2018).

303

304 Glacial oxygen change expands the volume of hypoxic waters (defined here as $[O_2]$ <80 mmol m^{-3}) below 1000 m depth, such

305 that the simulated global volume increases from the present value of 120 Mkm^3 to 237 Mkm^3 in LGM_all. Significant

306 expansion occurs in the deep Pacific and Indian oceans (Fig. 8), with hypoxic waters also appearing in the upper SO in the

307 Pacific sector, consistent with proxy records (Hoogakker et al., 2018; Lu et al., 2016). Because hypoxic conditions are lethal

308 for more than one-half of marine benthic animals (Vaquer-Sunyer and Duarte, 2008), expansion of hypoxic water in the deep

309 ocean can have an adverse impact on benthic fauna. Determining the biotic responses to glacial expansion of hypoxic water

310 would be helpful for understanding the biotic response to future deoxygenation associated with global warming.

311

312 Finally, we discuss the underestimation of deoxygenation in the deep SO in LGM_all. Because simulated changes in the

313 biological pump and sea-ice distributions are consistent with reconstructions (Obase et al., 2017), we then addressed circulation

314 changes. The simulated water mass age of the deep SO is younger during the LGM than during the PI by ~200 years (Fig. 7f),

315 indicating an increase in ventilation. However, $\Delta^{14}C$ records show an increase in water mass age of more than 1000 years, and

316 thus increased stratification (Skinner et al., 2010; Burke and Robinson, 2012). Enhanced mixing of surface waters with deep

317 waters supplies oxygen-rich surface waters to the deep ocean and simultaneously releases carbon accumulated in the deep

318 water to the atmosphere. Therefore, we attribute the underestimation of deoxygenation and carbon accumulation in the deep

319 SO to overestimated ventilation. Our results suggest that a stratified SO is required for reproducing glacial CO_2 drawdown and

320 oxygen decline in the deep SO, consistent with recent paleo-proxy data and models (Fischer et al., 2010; Sigman et al., 2010;

321 Kobayashi et al., 2015; Menviel et al., 2017). Menviel et al (2017) showed that weaker and shallower North Atlantic Deep

322 Water and weaker AABW could be necessary to reproduce the LGM oceanic $\delta^{13}C$ and radiocarbon distribution.

323

324 **4 Conclusion and remarks**

325   We quantified the impacts on glacial deoxygenation and CO_2 decreases caused by glaciogenic dust with higher iron solubility

326   and increase in nutrient inventory associated with a sea-level drop using the coupled atmosphere–ocean general circulation

327   model, aerosol model, and ocean biogeochemical model. As a result, we successfully reproduced the magnitude and large-

328   scale pattern of the observed oxygen change between the present and LGM. Our results show that iron fertilization from

329   glaciogenic dust and an increase in nutrient inventory could explain a glacial CO_2 decline of more than 30 ppm and

330   approximately one-half of deep ocean deoxygenation. These results also demonstrate the usefulness of the quantitative model-

331   proxy comparison of oxygen change in understanding glacial-interglacial CO_2 change. However, large uncertainty remains

332   because of the limited number of proxy data of quantitative oxygen change. Thus, we anticipate our findings will encourage

333   studies to obtain further qualitative and quantitative reconstructions from throughout the global deep ocean. A comparison

334   between the models and other proxy data (e.g. $\delta^{13}C$, (Schmittner and Somes, 2016)) is also required to obtain a more robust

335   and comprehensive understanding of the glacial carbon cycle.

336

337   The changes in nutrient inventory during the LGM have large uncertainties. Previous studies estimate that the oceanic PO_4 and

338   NO_3 inventories could have been 15–40% (Tamburini and Föllmi, 2009; Wallmann et al., 2016) and 10-100% (Deutsch et al.,

339   2004; Eugster et al., 2013; Somes et al., 2017) greater during glacial compared to interglacial periods, respectively. Moreover,

340   Somes et al. (2017) shows that sedimentary $\delta^{15}N$ records provide no constrain on this effect. Future simulations should test the

341   biogeochemical sensitivity to nutrient inventory changes.

342

343   We focused on the impacts of DFe flux changes from the dust on glacial CO_2 drawdown and deoxygenation in this study.

344   However, changes in the sedimentary and hydrothermal DFe flux and ligand concentration that are not considered in this study

345   could also be important. A glacial sea-level drop decreases the sedimentary DFe flux due to the continental shelf reduction.

346   However, the hydrothermal DFe flux is increased by the lower sea level and bottom pressure (Middleton et al., 2016). Muglia

347   et al. (2017) show that the changes in sedimentary and hydrothermal DFe flux associated with a sea-level drop increase CO_2

348   by 15 ppm and decrease CO_2 by 6 ppm, respectively. Although sedimentary DFe flux is proportional to the organic carbon

349   flux reaching the seafloor in our model, a parametrization with the Dfe flux as a function of organic carbon flux and bottom

15

350   oxygen concentrations is proposed in Dale et al. (2015). Glacial deep-water deoxygenation would increase sedimentary DFe

351   flux, leading to a further CO_2 decrease via the biological pump. Ligand concentrations strongly control DFe concentrations

352   (Gledhill and Buck, 2012). Because the ligand concentration is affected by numerous factors (Völker and Tagliabue, 2015),

353   changes in ligand concentration from the PI to LGM have large uncertainty. Thus, we quantified the effect of DFe flux changes

354   under a constant ligand concentration in the PI and LGM simulations. Changes in the sedimentary and hydrothermal DFe flux

355   and ligand concentration should be the subject of future research.

356

357   Our model-proxy comparison shows the importance of the combination of a more sluggish SO circulation and enhanced

358   biological transport of organic matter in the increased accumulation of respired carbon and deoxygenation in the deep SO.

359   However, present climate models cannot reproduce the stratified SO. A possible reason is that they are too coarse to capture

360   the process of dense water formation on the Antarctic shelf and tend to underestimate the strength of stratification in the SO

361   (Heuzé et al., 2013). The brine rejection process and/or change in the vertical diffusion coefficient could be necessary to

362   reproduce the stratified SO (Kobayashi et al., 2015; Bouttes et al., 2011). Similar to glacial oxygen changes, changes in ocean

363   circulation in the SO are crucial in projecting future oxygen changes associated with global warming (Yamamoto et al., 2015).

364   Therefore, an understanding of glacial oxygen changes will aid in better understanding and predicting future oxygen changes.

365

380   **References**

381   Albani, S., Mahowald, N. M., Perry, A. T., Scanza, R. A., Zender, C. S., Heavens, N. G., Maggi, V., Kok, J. F., and Otto-

382   Bliesner, B. L.: Improved dust representation in the Community Atmosphere Model., J. Adv. Model. Earth Sy., 6,

383   541–570, https://doi.org/10.1002/2013ms000279, 2014.

384   Bopp, L., Kohfeld, K. E., and Le Qu´er´e, C.: Dust impact on marine biota and atmospheric CO_2 during glacial periods,

385   Paleoceanography, 18, 1046, doi:10.1029/2002PA000810, 2003.

386   Bopp, L., Resplandy, L., Orr, J. C., Doney, S. C., Dunne, J. P., Gehlen, M., Halloran, P., Heinze, C., Ilyina, T., Séférian, R.,

387   Tjiputra, J., and Vichi, M.: Multiple stressors of ocean ecosystems in the 21st century: projections with CMIP5

388   models, Biogeosciences, 10, 6225–6245, https://doi.org/10.5194/bg-10-6225-2013, 2013.

389 Bopp, L., Resplandy, L., Untersee, A., Le Mezo, P., and Kageyama, M.: Ocean (de)oxygenation from the Last Glacial

390   Maximum to the twenty-first century: insights from Earth System models, Philos. T. Roy. Soc. Lond. A, 375, 2102,

391   https://doi.org/10.1098/rsta.2016.0323, 2017.

392 Bouttes, N., Paillard, D., Roche, D. M., Brovkin, V., and Bopp, L.: Last Glacial Maximum CO_2 and _13C successfully

393   reconciled, Geophys. Res. Lett., 38, L02705, doi:10.1029/2010gl044499, 2011.

394 Braconnot, P., Otto-Bliesner, B., Harrison, S., Joussaume, S., Peterchmitt, J.-Y., Abe-Ouchi, A., Crucifix, M., Driesschaert,

395   E., Fichefet, Th., Hewitt, C. D., Kageyama, M., Kitoh, A., Laîné, A., Loutre, M.-F., Marti, O., Merkel, U., Ramstein,

396   G., Valdes, P., Weber, S. L., Yu, Y., and Zhao, Y.: Results of PMIP2 coupled simulations of the Mid-Holocene and

397   Last Glacial Maximum – Part 1: experiments and large-scale features, Clim. Past, 3, 261–277, doi:10.5194/cp-3-

398   261-2007, 2007.

399 Broecker, W. S.: Glacial to interglacial changes in ocean chemistry, Progress in Oceanography, 11, 151–197,

400   doi:10.1016/0079-6611(82)90007-6, 1982.

401 Brovkin, V., Ganopolski, A., Archer, D., and Munhoven, G.: Glacial CO_2 cycle as a succession of key physical and

402   biogeochemical processes, Clim. Past, 8, 251-264, https://doi.org/10.5194/cp-8-251-2012, 2012.

403 Buchanan, P. J., Matear, R. J., Lenton, A., Phipps, S. J., Chase, Z., and Etheridge, D. M.: The simulated climate of the Last

404   Glacial Maximum and insights into the global marine carbon cycle, Clim. Past, 12, 2271-2295,

405   https://doi.org/10.5194/cp-12-2271-2016, 2016.

406 Bunzel, D., Schmiedl, G., Lindhorst, S., Mackensen, A., Reolid, J., Romahn, S., and Betzler, C.: A multi-proxy analysis of

407   Late Quaternary ocean and climate variability for the Maldives, Inner Sea, Clim. Past, 13, 1791-1813,

408   https://doi.org/10.5194/cp-13-1791-2017, 2017.

409 Burke, A. and Robinson, L. F.: The Southern Ocean's role in carbon exchange during the last deglaciation, Science, 335,

410   557–561, 2012.

411 Chikamoto, M. O., Abe-Ouchi, A., Oka, A., Ohgaito, R., and Timmermann, A.: Quantifying the ocean's role in glacial CO_2

412   reductions, Clim. Past, 8, 545-563, https://doi.org/10.5194/cp-8-545-2012, 2012.

413 Ciais, P., Sabine, C., Bala, G., Bopp, L., Brovkin, V., Canadell, J., Chhabra, A., DeFries, R., Galloway, J., Heimann, M.,

414   Jones, C., Le Quéré, C., Myneni, R. B., Piao, S., and Thornton, P.: Carbon and Other Biogeochemical Cycles, in:

415   Climate Change 2013: The Physical Science Basis. Contribution of Working Group I to the Fifth Assessment Report

416   of the Intergovernmental Panel on Climate Change, edited by: Stocker, T. F., Qin, D., Plattner, G.-K., Tignor, M.,

417   Allen, S. K., Boschung, J., Nauels, A., Xia, Y., Bex, V., and Midgley, P. M., Cambridge University Press,

418   Cambridge, United Kingdom and New York, NY, USA, 465– 570, 2013.

419 Conway, T., Wolff, E., Roethlisberger, R., Mulvaney, R., and Elderfield, H.: Constraints on soluble aerosol iron flux to the

420   Southern Ocean at the Last Glacial Maximum, Nature Communications, 6, 1–9, doi:10.1038/ncomms8850, 2015.

421 Curry,W. B. and Oppo, D.W.: Glacial water mass geometry and the distribution of $\delta^{13}C$ of CO_2 in the western Atlantic

422   Ocean, Paleoceanography, 20, PA1017, doi:10.1029/2004PA001021, 2005.

423 Deutsch, C., Sigman, D. M., Thunell, R. C., Meckler, A. N., and Haug, G. H.: Isotopic constraints on glacial/interglacial

424   changes in the oceanic nitrogen budget, Global Biogeochem. Cy., 18, GB4012, doi:10.1029/2003GB002189, 2004.

425 Diaz, R. J. and Rosenberg, R.: Spreading dead zones and consequences for marine ecosystems, Science, 321, 926–929, 2008.

426 Durand, A.,Chase, Z., Noble, T. L., Bostock, H., Jaccard, S. L., Townsend, A. T., Bindoff, N. L., Neil, H., and Jacobsen, G.:

427   Reduced oxygenation at intermediate depth of the southwest Pacific during the last glacial maximum, Earth Planet.

428   Sc. Lett., 491, 48-57, 2018.

429 Duteil, O., Koeve, W., Oschlies, A., Bianchi, D., Galbraith, E., Kriest, I., and Matear R.: A novel estimate of ocean oxygen

430   utilisation points to a reduced rate of respiration in the ocean interior, Biogeosciences, 10(11), 7723-7738, doi:

431   10.5194/bg-10-7723-2013, 2013.

432 Eppley, R. W.: Temperature and phytoplankton growth in the sea, Fish. B.-NOAA, 70, 1063–1085, 1972.

433 Eugster, O., Gruber, N., Deutsch, C., Jaccard, S. L., and Payne, M. R.: The dynamics of the marine nitrogen cycle across the

434   last deglaciation, Paleoceanography, 28, 116–129, doi:10.1002/palo.20020, 2013.

435 Fischer, H., Schmitt, J., Luthi, D., Stocker, T. F., Tschumi, T., Parekh, P., Joos, F., Kohler, P., Volker, C., Gersonde, R.,

436   Barbante, C., Le Floch, M., Raynaud, D., and Wolff, E.: The role of Southern Ocean processes in orbital and

437   millennial CO2 variations – a synthesis, Quaternary Sci. Rev., 29, 193–205, 2010.

438 Galbraith, E. and de Lavergne, C.: Response of a comprehensive climate model to a broad range of external forcings:

439   relevance for deep ocean ventilation and the development of late Cenozoic ice ages, Clim. Dynam.,

440   https://doi.org/10.1007/s00382-018-4157-8, 2018.

441 Galbraith, E. D. and Jaccard, S. L.: Deglacial weakening of the oceanic soft tissue pump: global constraints from

442   sedimentary nitrogen isotopes and oxygenation proxies, Quaternary Sci. Rev., 109, 38–48,

443   doi:10.1016/j.quascirev.2014.11.012, 2015.

444 Garcia, H. E., Locarnini, R., Boyer, T., Antonov, J., Baranova, O., Zweng, M., and Johnson, D.: Volume 3: Dissolved

445   Oxygen, Apparent Oxygen Utilization, and Oxygen Saturation,World Ocean Atlas 2009, S. Levitus, Ed. NOAA

446   Atlas NESDIS 70, US Government Printing Office, Washington, DC, 344 pp., 2010a.

447 Garcia, H. E., Locarnini, R., Boyer, T., Antonov, J., Zweng, M., Baranova, O., and Johnson, D.: Volume 4: Nutrients

448   (phosphate, nitrate, silicate), World Ocean Atlas 2009, edited by: Levitus, S., NOAA Atlas NESDIS 71, US

449   Government Printing Office, Washington, DC, 398 pp., 2010b.

450 Gledhill, M. and Buck, K.: The organic complexation of iron in the marine environment: a review, Frontiers in

451   Microbiology, 3, 1–17, doi:10.3389/fmicb.2012.00069, 2012.

452 Gottschalk, J., Skinner, L. C., Lippold, J., Vogel, H., Frank, N., Jaccard, S. L., and Waelbroeck, C.: Biological and physical

453   controls in the Southern Ocean on past millennial-scale atmospheric CO_2 changes, Nat. Commun., 7, 11539,

454   doi:10.1038/ncomms11539,2016.

455 Heinze, C., Hoogakker, B. A. A., and Winguth, A.: Ocean carbon cycling during the past 130 000 years – a pilot study on

456   inverse palaeoclimate record modelling, Clim. Past, 12, 1949-1978, https://doi.org/10.5194/cp-12-1949-2016, 2016.

457 Heuzé, C., Heywood, K. J., Stevens, D. P., and Ridley, J. K.: Southern Ocean bottom water characteristics in CMIP5 models,

458   Geophys. Res. Lett., 40, 1409–1414, doi:10.1002/grl.50287, 2013.

459 Hoogakker, B. A. A., Elderfield, H., Schmiedl, G., McCave, I. N., and Rickaby, R. E. M.: Glacial–interglacial changes in

460   bottom water oxygen content on the Portuguese margin, Nat. Geosci., 8, 40–43, doi:10.1038/ngeo2317, 2015.

Hoogakker, B. A. A., Lu, Z., Umling, N., Jones, L., Zhou, X., Rickaby, R. E. M., Thunell, R., Cartapanis, O., and Galbraith, E.: Glacial expansion of oxygen-depleted seawater in the eastern tropical Pacific. Nature, 562 (7727), 410-413. 10.1038/s41586-018-0589-x, 2018.

Ito, A., Myriokefalitakis, S., Kanakidou, M., Mahowald, N. M., Scanza, R. A., Hamilton, D. S., Baker, A. R., Jickells, T., Sarin, M., Bikkina, S., Gao, Y., Shelley, R. U., Buck, C. S., Landing, W. M., Bowie, A. R., Perron, M. M. G., Guieu, C., Meskhidze, N., Johnson, M. S., Feng, Y., Kok, J. F., Nenes, A., and Duce, R. A.: Pyrogenic iron: The missing link to high iron solubility in aerosols, Sci. Adv., 5, eaau7671, doi: 10.1126/sciadv.aau7671, 2019.

Ito, T. and Follows, M. J.: Preformed phosphate, soft tissue pump and atmospheric CO_2, J. Mar. Res., 63, 813–839, 2005.

Jaccard, S. L. and Galbraith, E. D.: Large climate-driven changes of oceanic oxygen concentrations during the last deglaciation, Nat. Geosci., 5, 151–156, doi:10.1038/ngeo1352, 2012.

Jaccard, S. L., Hayes, C. T., Hodell, D. A., Anderson, R. F., Sigman, D. M., and Haug, G. H.: Two modes of change in Southern Ocean productivity over the past million years, Science, 339, 1419–1423, 2013.

Jaccard, S. L., Galbraith, E. D., Martínez-García, A., and Anderson, R. F.: Covariation of deep Southern Ocean oxygenation and atmospheric CO_2 through the last ice age, Nature, 530, 207–10, doi:10.1038/nature16514, 2016.

Khatiwala, S., Schmittner, A., and Muglia, J.: Air-sea disequilibrium enhances ocean carbon storage during glacial periods, Sci. Adv., accepted.

Key, R. M., Kozyr, A., Sabine, C. L., Lee, K., Wanninkhof, R., Bullister, J. L., Feely, R. A., Millero, F. J., Mordy, C., and Peng, T.-H.: A global ocean carbon climatology: Results from Global Data Analysis Project (GLODAP), Global Biogeochem. Cy., 18, GB4031, https://doi.org/10.1029/2004GB002247, 2004.

Kobayashi, H., Abe-Ouchi, A., and Oka, A.: Role of Southern Ocean stratification in glacial atmospheric CO2 reduction evaluated by a three-dimensional ocean general circulation model, Paleoceanography, 30, 1202–1216, 2015.

Kobayashi, H., and Oka, A.: Response of atmospheric pCO2 to glacial changes in the Southern Ocean amplified by carbonate compensation. Paleoceanography 33, 1206-1229, 2018.

Kohfeld, K. E., Le Quéré, C., Harrison, S. P., and Anderson, R. F.: Role of marine biology in glacial-interglacial CO2 cycles, Science, 308, 74–78, doi:10.1126/science.1105375, 2005.

Kohfeld, K. E., Graham, R. M., De Boer, A. M., Sime, L. C., Wolff, E. W., Le Quere, C., and Bopp, L.: Southern Hemisphere westerly wind changes during the Last Glacial Maximum: paleo-data synthesis, Quaternary Sci. Rev., 68, 76–95, https://doi.org/10.1016/j.quascirev.2013.01.017, 2013.

Lambert, F., Tagliabue, A., Shaffer, G., Lamy, F., Winckler, G., Farias, L., Gallardo, L., and De Pol-Holz, R.: Dust fluxes and iron fertilization in Holocene and Last Glacial Maximum climates, Geophys. Res. Lett., 42, 6014–6023, doi:10.1002/2015gl064250, 2015.

Lu, Z., Hoogakker, B. A. A., Hillenbrand, C.-D., Zhou, X., Thomas, E., Gutchess, K. M., Lu, W., Jones, L., and Rickaby, R. E. M.: Oxygen depletion recorded in upper waters of the glacial Southern Ocean, Nat. Commun., 7, 11146, https://doi.org/10.1038/ncomms11146, 2015.

Mahowald, N. M., Muhs, D. R., Levis, S., Rasch, P. J., Yoshioka, M., Zender, C. S., and Luo, C.: Change in atmospheric mineral aerosols in response to climate: last glacial period, preindustrial, modern, and doubled carbon dioxide climates, J. Geophys. Res., 111, D10202, doi:10.1029/2005JD006653, 2006.

Marinov, I., Gnanadesikan, A., Sarmiento, J. L., Toggweiler, J. R., Follows, M., and Mignone, B. K.: Impact of oceanic circulation on biological carbon storage in the ocean and atmospheric pCO2, Global Biogeochem. Cy. 22(3), GB3007, doi:10.1029/2007GB002958, 2008.

Martin, J. H.: Glacial-interglacial CO2 change: the iron hypothesis, Paleoceanography, 5, 1–13, 1990.

Matsumoto, K.: Biology-mediated temperature control on atmospheric pCO$_2$ and ocean biogeochemistry, Geophys. Res. Lett., 34, L20605, https://doi.org/10.1029/2007GL031301, 2007.

Menviel, L., Joos, F., and Ritz, S. P.: Simulating atmospheric CO$_2$, ^{13}C and the marine carbon cycle during the Last Glacial–Interglacial cycle: possible role for a deepening of the mean remineralization depth and an increase in the oceanic nutrient inventory, Quat. Sci. Rev., 56, 46-68, 10.1016/j.quascirev.2012.09.012, 2012.

Menviel, L., Yu, J., Joos, F., Mouchet, A., Meissner, K., and England, M.: Poorly ventilated deep ocean at the Last Glacial Maximum inferred from carbon isotopes: A data-model comparison study, Paleoceanography, 32, 2–17, 2017.

509 Middleton, J. L., Langmuir, C. H., Mukhopadhyay, S., McManus, J. F., and Mitrovica, J. X.: Hydrothermal iron flux

510   variability following rapid sea level changes, Geophys. Res. Lett., 43, 3848–3856,

511   https://doi.org/10.1002/2016GL068408, 2016.

512 Moore, J. K. and Braucher, O.: Sedimentary and mineral dust sources of dissolved iron to the world ocean, Biogeosciences,

513   5, 631–656, doi:10.5194/bg-5-631-2008, 2008.

514 Moore, C. M., Mills, M. M., Arrigo, K. R., Berman-Frank, I., Bopp, L., Boyd, P. W., Galbraith, E. D., Geider, R. J., Guieu,

515   C., Jaccard, S. L., Jickells, T. D., La Roche, J., Lenton, T. M., Mahowald, N. M., Marañón, E., Marinov, I., Moore,

516   J. K., Nakatsuka, T., Oschilles, A., Saito, M. A., Thingstad, T. F., Tsuda, A., and Ulloa, O.: Processes and patterns of

517   oceanic nutrient limitation, Nat. Geosci., 6, 701–710,https://doi.org/10.1038/ngeo1765, 2013.

518 Muglia, J., Somes, C., Nickelsen, L., and Schmittner, A.: Combined effects of atmospheric and seafloor iron fluxes to the

519   glacial ocean. Paleoceanography 32, 1204–1218, 2017.

520 Muglia, J., Skinner, L. C., and Schmittner A.: Weak overturning circulation and high Southern Ocean nutrient utilization

521   maximized glacial ocean carbon, Earth Planet Sc Lett, 496, 47-56, doi: 10.1016/j.epsl.2018.05.038, 2018.

522 Obase, T., Abe-Ouchi, A., Kusahara, K., Hasumi, H., and Ohgaito, R.: Responses of basal melting of Antarctic ice shelves to

523   the climatic forcing of the Last Glacial Maximum and CO_2 doubling. J. Climate, 30, 3473–3497, 2017.

524 Ohgaito, R., Abe-Ouchi, A., O'ishi, R., Takemura, T., Ito, A., Hajima, T., Watanabe, S., and Kawamiya, M.: Effect of high

525   dust amount on surface temperature during the Last Glacial Maximum: a modelling study using MIROC-ESM,

526   Clim. Past, 14, 1565-1581, https://doi.org/10.5194/cp-14-1565-2018, 2018.

527 Oka, A., Abe-Ouchi, A., Chikamoto, M. O., and Ide, T.: Mechanisms controlling export production at the LGM: Effects of

528   changes in oceanic physical field and atmospheric dust deposition, Global Biogeochem. Cy., 25, GB2009,

529   doi:10.1029/2009GB003628, 2011.

530 Parekh, P., Follows, M. J., and Boyle, E. A.: Decoupling of iron and phosphate in the global ocean, Global Biogeochem. Cy.,

531   19, GB2020, doi:10.1029/2004GB002280, 2005.

532 Parekh, P., Follows, M. J., Dutkiewicz, S., and Ito, T.: Physical and biological regulation of the soft tissue carbon pump,

533   Paleoceanography, 21, PA3001, doi:10.1029/2005PA001258, 2006.

534 Parekh, P., Joos, F., and Muller, S. A.: A modeling assessment of the interplay between aeolian iron fluxes and ironbinding

535   ligands in controlling carbon dioxide fluctuations during Antarctic warm events, Paleoceanography, 23, Pa4202,

536   doi:10.1029/2007pa001531, 2008.

537 Roth, R., Ritz, S. P., and Joos, F.: Burial-nutrient feedbacks amplify the sensitivity of atmospheric carbon dioxide to changes

538   in organic matter remineralisation, Earth Syst. Dynam., 5, 321-343, 10.5194/esd-5-321-2014, 2014.

539 Russell, J. L., and Dickson, A. G.: Variability in oxygen and nutrients in South Pacific Antarctic Intermediate Water, Global

540   Biogeochem Cy, 17, doi:10.1029/2000gb001317, 2003.

541 Sarmiento, J. L., and Gruber, N.: Ocean Biogeochemical Dynamics, chap. 8, Carbon cycle, pp.318-358, Princeton Univ.

542   Press, Princeton, N. J, 2006.

543 Schmiedl, G. and Mackensen, A.: Multispecies stable isotopes of benthic foraminifers reveal past changes of organic matter

544   decomposition and deepwater oxygenation in the Arabian Sea, Paleoceanography, 21, 1–14,

545   doi:10.1029/2006PA001284, 2006.

546 Schmittner, A. and Somes, C. J.: Complementary constraints from carbon (C-13) and nitrogen (N-15) isotopes on the glacial

547   ocean's soft-tissue biological pump, Paleoceanography, 31, 669–693, 2016.

548 Schroth, A. W., Crusius, J., Sholkovitz, E. R., and Bostick, B. C.: Iron solubility driven by speciation in dust sources to the

549   ocean, Nat. Geosci., 2, 337–340, 2009.

550 Shoenfelt, E. M., Winckler, G., Lamy, F., Anderson, R. F., and Bostick, B. C.: Highly bioavailable dust-borne iron delivered

551   to the Southern Ocean during glacial periods. Proc. Natl. Acad. Sci. USA, 115, 11180-11185, 2018

552 Sigman, D. M., Hain, M. P., and Haug, G. H.: The polar ocean and glacial cycles in atmospheric CO_2 concentration, Nature,

553   466, 47–55, doi:10.1038/nature09149, 2010.

554 Skinner, L. C., Fallon, S., Waelbroeck, C., Michel, E., and Barker, S.: Ventilation of the deep Southern Ocean and deglacial

555   CO2 rise, Science, 328, 1147–1151, 2010.

556 Somes, C. J., Schmittner, A., Muglia, J., and Oschlies A.: A Three-Dimensional Model of the Marine Nitrogen Cycle during

557   the Last Glacial Maximum Constrained by Sedimentary Isotopes, Frontiers in Marine Science, 4,

558   doi:10.3389/fmars.2017.00108, 2017.

559 Tagliabue, A., Bopp, L., Dutay, J. C., Bowie, A. R., Chever, F., Jean-Baptiste, P., Bucciarelli, E., Lannuzel, D., Remenyi, T.,

560   Sarthou, G., Aumont, O., Gehlen, M., and Jeandel, C.: Hydrothermal contribution to the oceanic dissolved iron

561   inventory, Nat. Geosci., 3, 252–256, 2010.

562 Tagliabue, A., Bopp, L., Roche, D. M., Bouttes, N., Dutay, J.-C., Alkama, R., Kageyama, M., Michel, E., and Paillard, D.:

563   Quantifying the roles of ocean circulation and biogeochemistry in governing ocean carbon-13 and atmospheric

564   carbon dioxide at the last glacial maximum, Clim. Past, 5, 695-706, https://doi.org/10.5194/cp-5-695-2009, 2009.

565 Tamburini, F. and Föllmi, K. B.: Phosphorus burial in the ocean over glacial-interglacial time scales, Biogeosciences, 6,

566   501–513, doi:10.5194/bg-6-501-2009, 2009.

567 Tschumi, T., Joos, F., Gehlen, M., and Heinze, C.: Deep ocean ventilation, carbon isotopes, marine sedimentation and the

568   deglacial CO2 rise, Clim. Past, 7, 771-800, 10.5194/cp-7-771-2011, 2011.

569 Umling, N. E., and Thunell, R. C.: Mid-depth respired carbon storage and oxygenation of the eastern equatorial Pacific over

570   the last 25,000 years. Quaternary Science Reviews, 189, 43-56, 2018.

571 Vaquer-Sunyer, R. and Duarte, C. M.: Thresholds of hypoxia for marine biodiversity, Proc. Natl. Acad. Sci., 105, 15452–57,

572   2008.

573 Völker, C. and Tagliabue, A.: Modeling organic iron-binding ligands in a three-dimensional biogeochemical ocean model,

574   Mar. Chem., 173, 67–77, doi:10.1016/j.marchem.2014.11.008, 2015.

575 Wallmann, K., Schneider, B., and Sarnthein, M.: Effects of eustatic sea-level change, ocean dynamics, and nutrient

576   utilization on atmospheric $p\text{CO}_2$ and seawater composition over the last 130 000 years: a model study, Clim. Past,

577   12, 339-375, https://doi.org/10.5194/cp-12-339-2016, 2016.

578 Yamamoto, A., Abe-Ouchi, A., Shigemitsu, M., Oka, A., Takahashi, K., Ohgaito, R., and Yamanaka, Y.: Global deep ocean

579   oxygenation by enhanced ventilation in the Southern Ocean under longterm global warming, Global Biogeochem.

580   Cy., 29, 1801–1815, 2015.

581 Yamamoto, A., Abe-Ouchi, A., and Yamanaka, Y.: Long-term response of oceanic carbon uptake to global warming via

582   physical and biological pumps, Biogeosciences, 15, 4163-4180, https://doi.org/10.5194/bg-15-4163-2018, 2018.
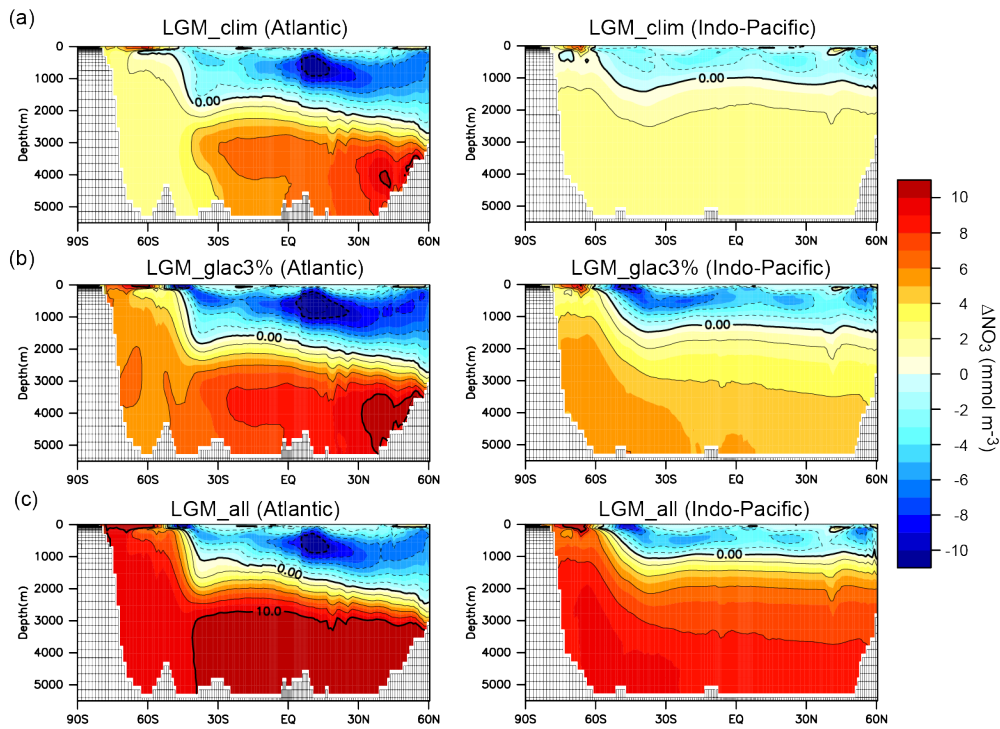
583

584

585
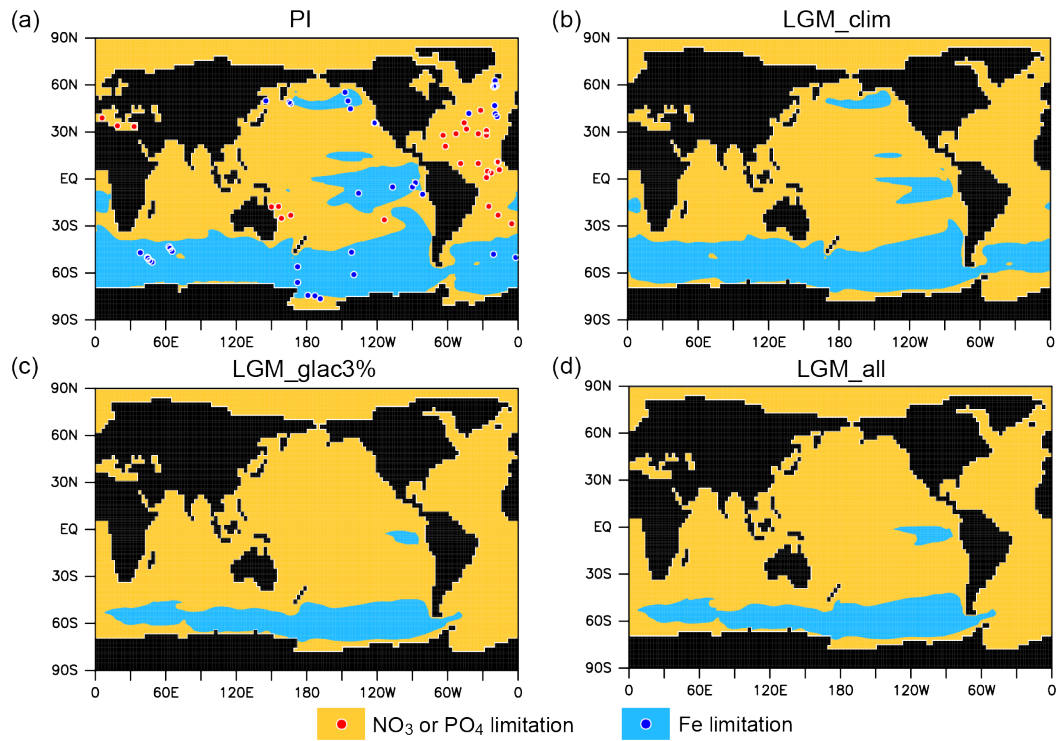
Figure 1. Primary limiting nutrient for phytoplankton for the (a) PI, (b) LGM_clim, (c)LGM_glac3%, and (d) LGM_all.

Shade indicates NO₃ or PO₄ limitation (orange) and Fe limitation (blue). Circles represent observed limiting nutrients from
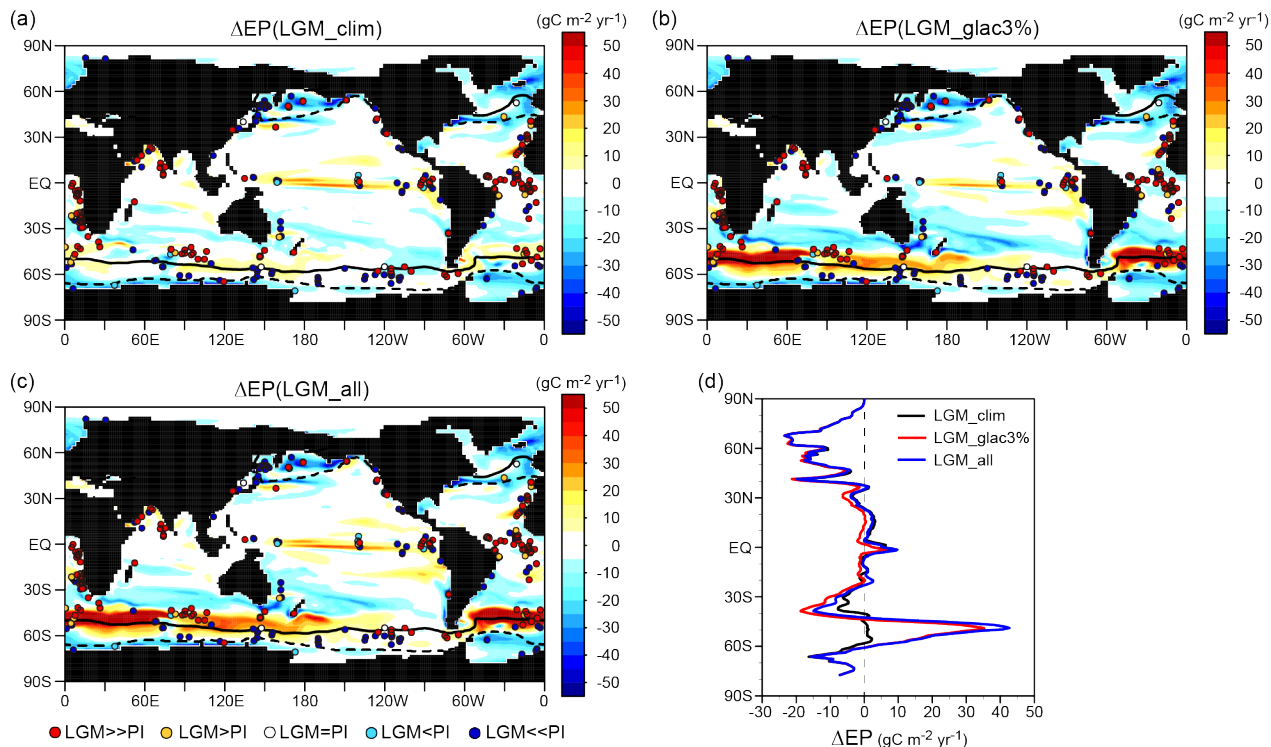
nutrient addition experiments (Moore et al., 2013).

591

Figure 2. NO$_3$ change resulting from changes in the climate and biological pump in LGM simulations. Zonal mean changes

in NO$_3$ from the PI to (a) LGM_clim, (b) LGM_glac3%, and (c) LGM_all. The left and right panels show the Atlantic and

Indo-Pacific oceans, respectively.

595

Figure 3. Model-proxy comparison of EP change from the PI to LGM. The EP difference from the PI for (a) LGM_clim, (b) LGM_glac3%, and (c) LGM_all. Circles show proxy data (Kohfeld et al., 2013). Solid (dotted) lines refer to the glacial sea ice fraction of 0.1 during August (February). (d) Zonal mean changes in the surface EP from the PI for LGM_clim (black), LGM_glac3% (red), and LGM_all (blue).
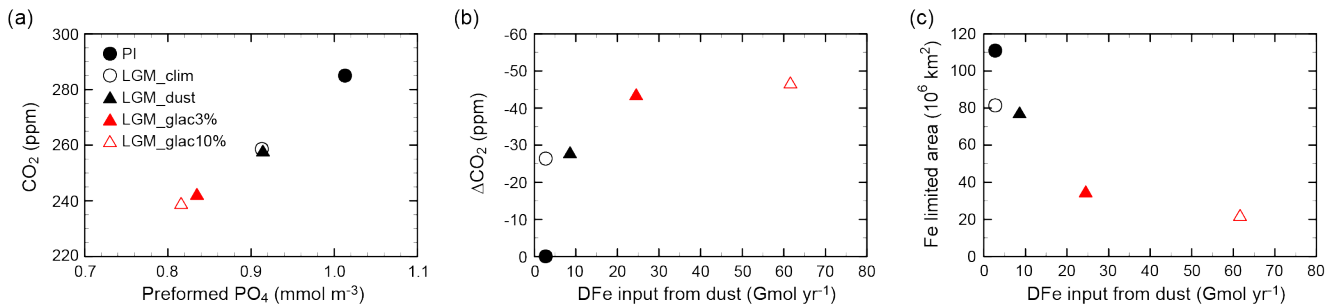
29
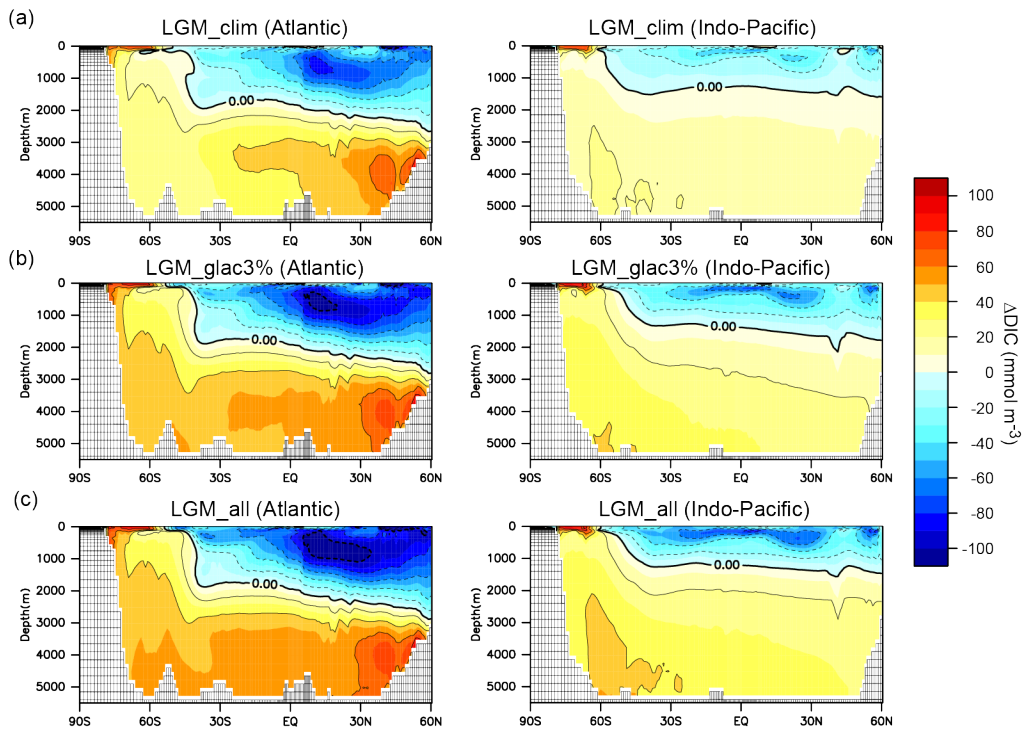
Figure 4. DIC change resulting from changes in the climate and biological pump in LGM simulations. Zonal mean changes in DIC from PI to (a) LGM_clim, (b) LGM_glac3%, and (c) LGM_all. The left and right panels show the Atlantic and Indo-Pacific oceans, respectively.


Figure 5. CO_2 change and its relationship to efficiency of the biological pump and iron cycle. (a) Atmospheric CO_2 as a function of globally averaged preformed PO_4. (b) Changes in CO_2 from the PI as a function of DFe input from dust. (c) Fe-limited area as a function of DFe input from dust. Shown are the PI (black filled circle), LGM_clim (black open circle), LGM_dust (black filled triangle), LGM_glac3% (red filled triangle), and LGM_glac10% (red open triangle).

30

612

613
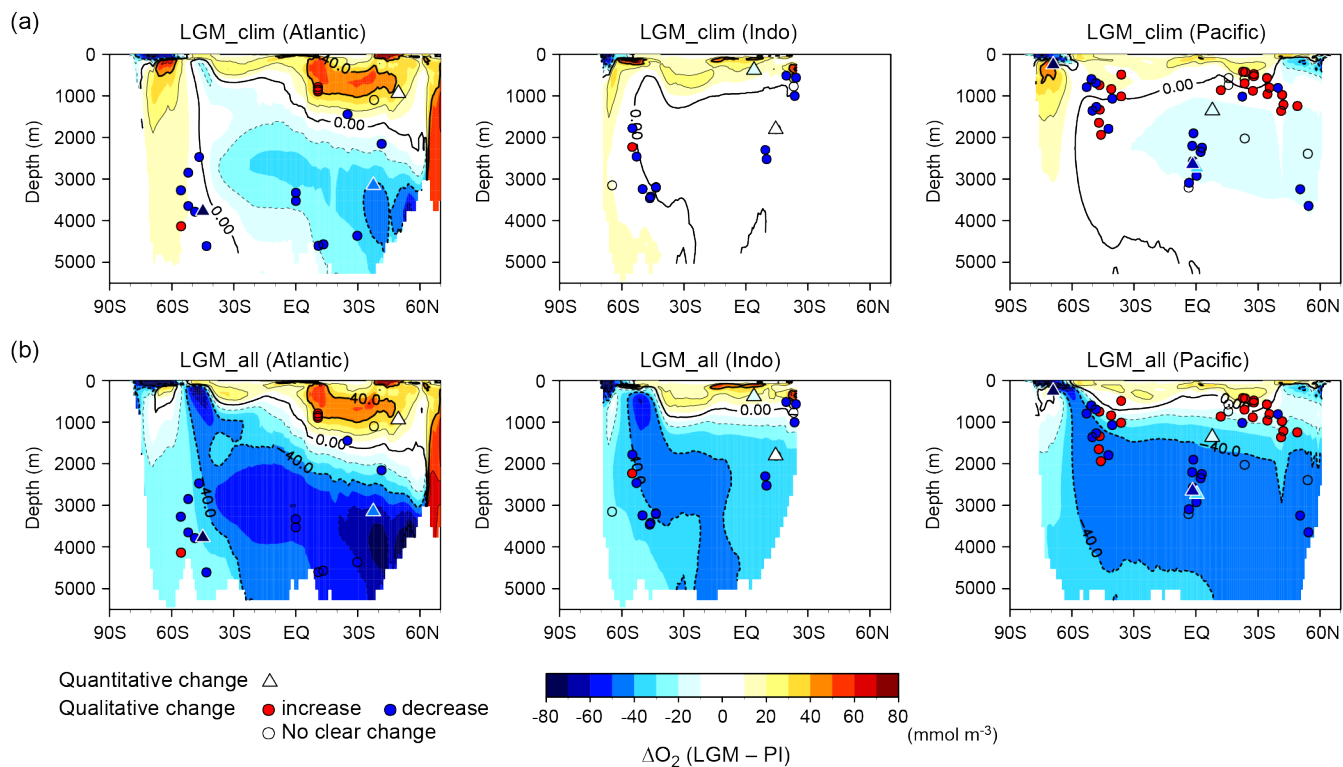
Figure 6. Model-proxy comparison of changes in dissolved oxygen concentration from the PI to LGM. Zonal mean changes in O_2 from the PI to (a) LGM_clim and (b) LGM_all for the Atlantic (left), Indian (middle), and Pacific (right) oceans; the contour interval is 20 mmol m^{-3}. Circles show proxy records of qualitative O_2 change from multi-proxy data compilation from Jaccard and Galbraith (2012) (except δ^{15}N data), Jaccard et al. (2016), and Durand et al. (2018). Red (blue) circles indicate O_2 increase (decrease) from the Holocene to LGM. Triangles show proxy records of quantitative O_2 change from (Schmiedl and Mackensen, 2006; Hoogakker et al., 2015, 2018; Gottschalk et al., 2016; Lu et al., 2016; Bunzel et al., 2017; Umling and Thunell, 2018) (triangles shaded using the same colour scale).

622

623

624
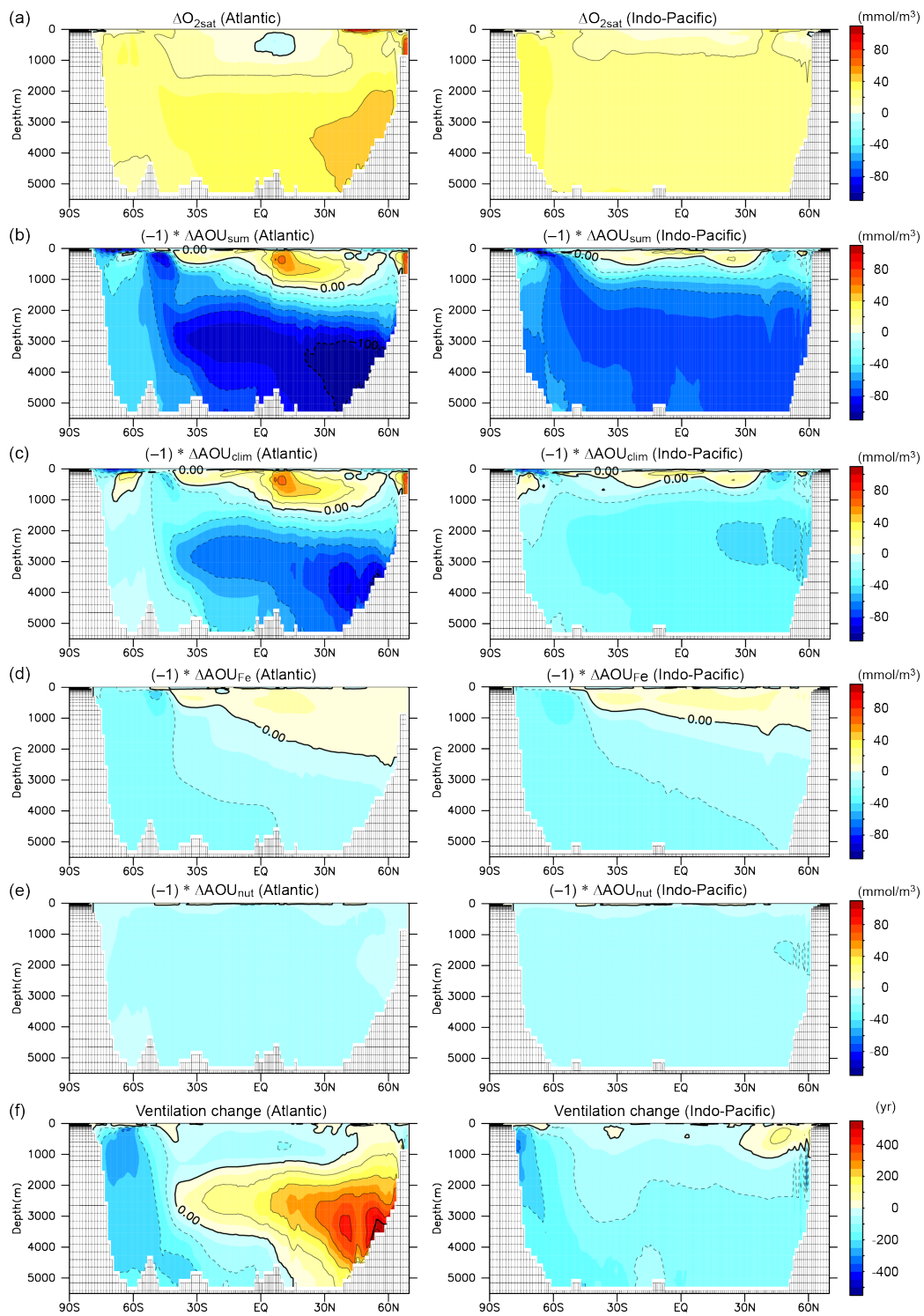
Figure 7. Contributions of individual mechanisms to oxygen change and ventilation change. Zonal mean changes of (a) O_{2sat},

(b) AOU_{sum}, (c) AOU_{clim}, (d) AOU_{Fe}, (e) AOU_{nut}, and (f) ventilation age from the PI to LGM. Left and right panels show the

Atlantic and Indo-Pacific oceans: the contour intervals are 20 mmol m^{-3} for (a)–(e) and 100 years for (f). We decomposed the

total AOU change ($\Delta AOU_{sum} = AOU_{(LGM\_all)} - AOU_{(PI)}$) into the effects of climate change ($\Delta AOU_{clim} = AOU_{(LGM\_clim)} -$

$AOU_{(PI)}$), iron fertilization ($\Delta AOU_{Fe} = AOU_{(LGM\_glac3\%)} - AOU_{(LGM\_clim)}$), and nutrient inventory increase ($\Delta AOUnut =$

$AOU_{(LGM\_all)} - AOU_{(LGM\_glac3\%)}$).
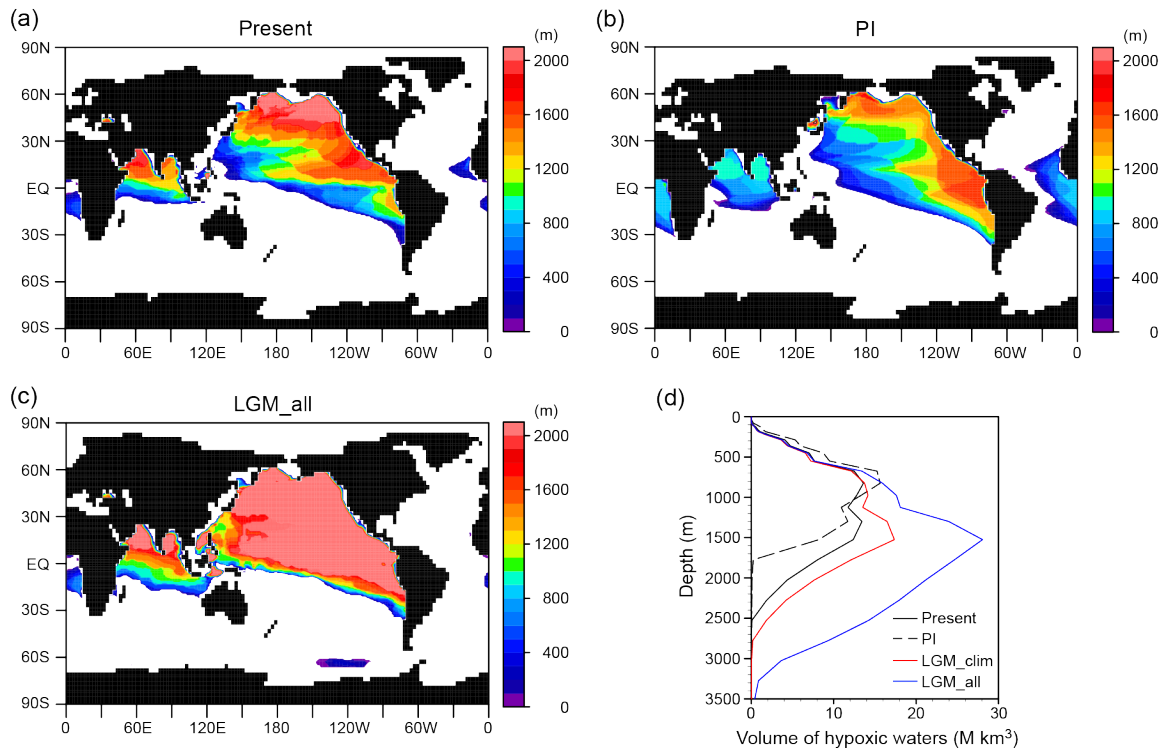
Figure 8. Hypoxic waters expansion. Horizontal distribution of thickness of the hypoxic waters ([O_2] <80 mmol m^{-3}) for the

(a) present, (b) PI, and (c) LGM_all. (d) Vertical distribution of hypoxic waters for the present (black solid), PI (black dashed),

LGM_clim (red), and LGM_all (blue). Because current coarse resolution models have difficulties reproducing low oxygen

concentration for the present day (Bopp et al., 2013), observed values from WOA2009 (Garcia et al., 2010a) were used for the

present. For the LGM simulations, we combined the observed values with the modelled changes.

Experiments	Climate	Dust deposition	Fe solubility in glaciogenic dust	Dust DFe (Gmol yr^{-1})	Global PO$_4$ (mmol m^{-3})
PI	PI	PI	-	2.7	2.13
LGM_clim	LGM	PI	-	2.7	2.2 (+3%)
LGM_dust	LGM	LGMctl	-	8.6	2.2 (+3%)
LGM_glac3%	LGM	LGMglac	3%	24.5	2.2 (+3%)
LGM_glac10%	LGM	LGMglac	10%	61.6	2.2 (+3%)
LGM_all	LGM	LGMglac	3%	24.5	2.45 (+15%)

639

640 Table 1. Description of the model experiments.

641

Experiments	Surface NO$_3$ (mmol m^{-3})	Surface DFe (μmol m^{-3})	Fe limited area (10^6 km^2)	Global ΔEP (Pg C yr^{-1})	ΔEP (>45°S) (Pg C yr^{-1})	ΔEP (<45°S) (Pg C yr^{-1})	Preformed PO$_4$ (mmol m^{-3})	ΔCO$_2$ (ppm)	ΔO$_{2\,deep}$ (mmo m^{-3})	ΔAOU$_{deep}$ (mmol m^{-3})
PI	7.7	0.38	111	(8.54)	(6.19)	(2.35)	1.013	(285)	(156)	(182.5)
LGM_clim	6.8	0.39	81	-0.54	-0.45	-0.09	0.913	-26.4	-7	37.3
LGM_dust	6.9	0.42	80	-0.54	-0.49	-0.05	0.914	-27.6	-8	38.9
LGM_glac3%	5.8	0.5	35	-0.54	-1.31	+0.77	0.835	-43.2	-28	58.7
LGM_glac10%	5.5	0.54	23	-0.54	-1.46	+0.92	0.816	-46.4	-33	63.6
LGM_all	6.5	0.48	39	+0.32	-0.63	+0.95	1.002	-59.2	-42	72.8

642

643 Table 2. Results of the model experiments. Simulated global average of surface NO$_3$, DFe, and Fe-limited area and changes in

644 EP at 100 m, atmospheric CO$_2$, and globally averaged preformed PO$_4$, O$_2$ and AOU below 2000 m depth from the PI. Values

645 in brackets are the PI results.